JAMES | Journal of Advances in Modeling Earth Systems

RESEARCH ARTICLE
10.1029/2024MS004625

Implementation of Sub-Grid Scale Temperature Perturbations Induced by Non-Orographic Gravity Waves in WACCM6

Simchan Yook[1], Susan Solomon[1], Michael Weimer[2], Douglas E. Kinnison[3], Rolando Garcia[3], and Kane Stone[1]

[1]Department of Earth, Atmospheric and Planetary Sciences, Massachusetts Institute of Technology, Cambridge, MA, USA, [2]Institute of Environmental Physics, University of Bremen, Bremen, Germany, [3]National Center for Atmospheric Research, Boulder, CO, USA

Key Points:

- We updated the subgrid-scale temperature parameterization to include non-orographic gravity waves from frontal activity and convection
- The non-orographic gravity waves increase the daytime variability of the ozone concentration, particularly in the lower mesosphere
- The non-orographic waves also enhance cirrus cloud formations in the upper troposphere across tropical to extratropical latitudes

Supporting Information:

Supporting Information may be found in the online version of this article.

Correspondence to:

S. Yook,
syook@mit.edu

Citation:

Yook, S., Solomon, S., Weimer, M., Kinnison, D. E., Garcia, R., & Stone, K. (2025). Implementation of sub-grid scale temperature perturbations induced by non-orographic gravity waves in WACCM6. *Journal of Advances in Modeling Earth Systems*, *17*, e2024MS004625. https://doi.org/10.1029/2024MS004625

Received 7 AUG 2024
Accepted 15 FEB 2025

Abstract Atmospheric gravity waves can play a significant role on atmospheric chemistry through temperature fluctuations. A recent modeling study introduced a method to implement subgrid-scale *orographic* gravity-wave-induced temperature perturbations in the Whole Atmosphere Community Climate Model (WACCM). The model with a wave-induced temperature parameterization was able to reproduce for example, the influence of mountain wave events on atmospheric chemistry, as highlighted in previous literature. Here we extend the subgrid-scale wave-induced temperature parameterization to also include *non-orographic* gravity waves arising from frontal activity and convection. We explore the impact of these waves on middle atmosphere chemistry, particularly focusing on reactions that are strongly sensitive to temperature. The non-orographic gravity waves increase the variability of chemical reaction rates, especially in the lower mesosphere. As an example, we show that this, in turn, leads to increases in the daytime ozone variability. To demonstrate another impact, we briefly investigate the role of non-orographic gravity waves in cirrus cloud formation in this model. Consistent with findings from the previous study focusing on orographic gravity waves, non-orographic waves also enhance homogeneous nucleation and increase cirrus clouds. The updated method used enables the global chemistry-climate model to account for both orographic and non-orographic gravity-wave-induced subgrid-scale dynamical perturbations in a consistent manner.

Plain Language Summary Atmospheric gravity waves can affect atmospheric chemistry by inducing temperature changes. A recent study improved the Whole Atmosphere Community Climate Model (WACCM) to better account for these temperature changes caused by orographic gravity waves. Here we extend the method to also account for non-orographic gravity waves from frontal activity and convection. With this updated method, the model now simulates how these waves (a) influence chemical reactions in the middle atmosphere, as well as (b) affect cirrus cloud formation in the upper troposphere. The updated method allows the model to consistently incorporate the effects of both mountain-related and other types of gravity waves.

1. Introduction

Atmospheric gravity waves play an important role in the dynamical and thermal structure of the middle atmosphere (Alexander et al., 2010; Andrews et al., 1987; Holton, 1983; Lindzen & Holton, 1968). Gravity waves arise from different sources including orography, convection and jet/frontal systems, propagate both horizontally and vertically in a thermally stratified atmosphere, and transport horizontal momentum and energy from the troposphere to the middle atmosphere (Dewan et al., 1998; Dörnbrack et al., 1999; Fritts & Nastrom, 1992; Jiang et al., 2005; Lilly & Kennedy, 1973; O'Sullivan and Dunkerton, 1995; Piani et al., 2000). The acceleration resulting from the dissipation of the gravity waves (i.e., gravity wave drag) is one of the primary drivers of the large-scale circulation and affects transport of chemicals in the middle atmosphere (Alexander et al., 2010; Andrews et al., 1987; Garcia & Solomon, 1985; Holton, 1983; Lindzen & Holton, 1968).

Gravity waves can also play a key role in photochemistry and microphysical processes in the atmosphere by changing atmospheric temperature and pressure. Wave-induced temperature fluctuations affect aerosol formation and growth (e.g., Borrmann et al., 1997; Meilinger et al., 1995; Peter et al., 1994; Tsias et al., 1997), polar stratospheric cloud formation (PSC; Carslaw et al., 1998a, 1998b), cirrus cloud formation (Jensen et al., 1996; Potter & Holton, 1995), and chemical reaction rates. This is because the chemical and microphysical processes

exhibit strong non-linear dependence on temperature (e.g., Carslaw et al., 1994; Meilinger et al., 1995; Tabazadeh et al., 1994; Tsias et al., 1997). Cooling from wave-like temperature fluctuations can lead to cloud formation even though the mean temperature averaged across the wave motion remains above the cloud formation threshold. Several heterogeneous reactions, such as chlorine activation occurring on the surface of aerosol and PSCs (Borrmann et al., 1997), as well as gas-phase reactions, such as thermal decomposition of the ClO dimer (McKenna et al., 1990), are non-linearly dependent on temperature. Thus, net chemical rates can be significantly affected by gravity waves.

In general, current climate models still do not have enough horizontal resolution to explicitly simulate the mesoscale and smaller scale gravity waves. Thus, the main effects of the unresolved gravity waves on large-scale circulation need to be parameterized if they are to be included (Holt et al., 2016; Jewtoukoff et al., 2015; Kim et al., 2003). Several gravity wave schemes have been developed to represent sub-grid scale orographic gravity wave drag in different climate models (Alexander & Ortland, 2010; Alpert, 2004; Kim et al., 2003; McFarlane, 1987). Orographic gravity wave parameterization in Community Earth System Model (CESM) has been developed based on the McFarlane theory, which assumes a two-dimensional steady-state hydrostatic wave with vertical propagation only (McFarlane, 1987). The CESM's orographic wave scheme has been improved to account for anisotropic orography including orientation, height, and size of orographic ridges (see Appendix B in Weimer et al., 2023).

Gravity wave parameterizations have also been developed to represent non-orographic gravity waves generated by two dominant sources: (a) convectively generated gravity waves based on the theoretical relationship between convective heating and wave momentum fluxes (Beres et al., 2004, 2005; Bushell et al., 2015; Chun & Kim, 2008), and (b) frontally generated gravity waves using the frontogenesis function (Hoskins, 1982) as a diagnostic for wave momentum flux induced by frontal activity (Charron & Manzini, 2002; Richter et al., 2010, 2014).

In global climate models, implementing the unresolved gravity wave perturbations in chemical and microphysical processes has been considered challenging; however, some studies have developed parameterizations of the sub-grid scale perturbations on cirrus formation (Barahona et al., 2017; Dean et al., 2007; Lyu et al., 2023; Penner et al., 2018), as well as PSC formation and middle atmospheric chemistry (Orr et al., 2020; Weimer et al., 2021, 2023).

Two recent studies, Weimer et al. (2023) and Lyu et al. (2023), developed a similar method to account for the temperature and vertical velocity fluctuations induced by sub-grid scale gravity waves in the Community Earth System Model version 2 (CESM2; Danabasoglu et al., 2020). They both estimated the amplitude of wave-induced fluctuations based on parameterized wave momentum fluxes from *orographic* gravity-wave schemes and grid-scale dynamical fields (temperature and wind fields). Weimer et al. (2023) converted the sub-grid scale wave momentum flux to temperature fluctuations and included them in the chemistry, and Lyu et al. (2023) applied the vertical velocity fluctuations to the microphysics of cirrus cloud formation. While Weimer et al. (2023) and Lyu et al. (2023) mainly focused on the role of orographic waves, it has been suggested that gravity waves originating from non-orographic sources can also play an important role in global atmospheric circulation, as well as in chemical and microphysical processes (e.g., Dinh et al., 2016; Kärcher & Ström, 2003; Schoeberl et al., 2016; Wright, 2019; Zou et al., 2021).

Building on the method from previous studies, we aim to account for the sub-grid scale dynamical fluctuations induced by gravity waves from different sources including *non-orographic* gravity waves arising from frontal activity and convection. Then, we explore examples of their role in global atmospheric modeling. Section 2 describes the model, experiments, and method to estimate the amplitude of sub-grid scale temperature fluctuations. Section 3 explores the impacts of the gravity waves on example chemical concentrations and ice clouds. Section 4 summarizes the results and discusses future implications.

2. Method

2.1. WACCM6

The Whole Atmosphere Community Climate Model (WACCM6) of the Community Earth System Model (CESM2.1) is used in this study (Danabasoglu et al., 2020; Gettelman et al., 2019). The FWSD compset (refer to Gettelman et al., 2019) based on the Specified Dynamics (SD) version of the model (Davis et al., 2022) with a

relaxation time of 50 hr is used following Weimer et al. (2023). Thus, in all experiments, the modeled winds and temperatures between the surface to 1 hPa are relaxed toward reference meteorology from Modern-Era Retrospective Analysis for Research and Applications version 2 (MERRA2, Gelaro et al., 2017). The chemistry scheme for WACCM includes detailed chemistry for the Troposphere, Stratosphere, Mesosphere and Lower Thermosphere (TSMLT scheme) and includes 158 photochemical species, 117 photolysis reactions, 331 gas-phase reactions, 2 aqueous-phase reactions, and 10 heterogeneous reactions (Emmons et al., 2010; Kinnison et al., 2007; Marsh et al., 2013; Mills et al., 2016). The SD-WACCM simulations are run with a horizontal resolution of $1.25° \times 0.9°$, 88 vertical levels, a model top at about 140 km, and prescribed ocean and ice models.

2.2. Parameterization of Non-Orographic Gravity Waves in WACCM6

The non-orographic gravity wave parameterization in WACCM6 includes separate source specifications of convective and frontal gravity waves (Gettelman et al., 2019; Richter et al., 2010). The convective gravity wave parameterization employs the "Beres scheme" to specify the gravity wave source spectrum (Beres et al., 2004, 2005). The model's deep convection parameterization scheme (Zhang & McFarlane, 1995) provides information about the depth and rate of convective heating, and then the phase speed spectrum of gravity wave momentum flux is determined by the Beres scheme based on the convective heating rate and the mean horizontal wind in the heating region. Thus, the convective gravity wave source specification in WACCM6 is coupled to the model's internal representation of convective processes. The convective gravity waves generated by the Beres scheme in WACCM6 were validated using tropical observations (Alexander et al., 2021).

The frontal gravity wave source specification is based on the frontogenesis function (Hoskins, 1982; Miller, 1948). At each time step, the frontogenesis function is calculated using information about the dynamical fields at a 600 hPa level, which corresponds to a typical steering level of fronts (Charron & Manzini, 2002). Then, the frontal gravity waves are launched in all grid points where the frontogenesis function at 600 hPa exceeds a specific threshold (Richter et al., 2010).

2.3. Sub-Grid Scale Dynamical Fluctuations Due To Gravity Waves

We provide a brief summary of the subgrid-scale temperature parameterization and the sub-stepping method (for details see Weimer et al., 2023). The peak wave displacement amplitude ($\hat{\delta}$) is calculated based on the wave properties, including wave momentum flux (τ), phase speed, and wavelength derived from the wave drag scheme and other information about the background dynamical fields as follows (Lindzen, 1981),

$$\hat{\delta} = \sqrt{\frac{\tau}{\rho N \left| \overline{U} - c \right| k_h}}, \tag{1}$$

where $\rho, N, \overline{U}, c$ and k_h denotes air density, the Brunt-Vaisala frequency, horizontal wind speed, wave phase speed, and the horizontal wave number, respectively. Then, the amplitude of temperature fluctuation ($\hat{T}$) by the subgrid-scale gravity wave is estimated using the peak wave displacement amplitude as follows,

$$\left| \hat{T} \right| = S\hat{\delta}, \tag{2}$$

where S denotes the static stability.

Our method for estimating temperature fluctuation closely follows that outlined in Weimer et al. (2023), except for the following differences in how we estimate the total momentum flux. For orographic waves, Weimer et al. (2023) used a single vertical wavenumber component corresponding to the largest amplitude to estimate the peak wave displacement. However, for non-orographic gravity waves, we used a full spectrum of vertical wavenumbers after applying few simplifications. Although it is well known that complex wave-wave interactions among waves with different wavenumbers significantly influence the shape and evolution of the total gravity wave spectrum (Fritts & Alexander, 2003), we simplify the total momentum flux of the wave spectrum by summing momentum fluxes over a phase speed spectrum in each cardinal direction, and then selecting the direction with the highest magnitude. The peak wave displacement $\left(\hat{\delta}\right)$ is calculated using the total momentum flux (τ) at each grid point, together with the vertical wavenumber corresponding to the maximum momentum flux in

the spectrum and background dynamical fields. We acknowledge that our calculations involve certain simplifications, such as selecting a single vertical wavenumber corresponding to the maximum momentum flux, rather than accounting for the superposition of different wavenumbers. The results are not sensitive to the simplification of using a single vertical wavenumber corresponding to the maximum momentum flux instead of the full spectrum of phase speeds, for the peak wave displacement calculation (Figure S1 in Supporting Information S1). In future work, applying a scaling approach similar to that in Weimer et al. (2023) by comparing with observations could help reduce model biases in the amplitude of wave-induced temperature fluctuations.

Following Lyu et al. (2023), we estimate subgrid-scale vertical velocity variances (σ_w^2) as below,

$$\sigma_w^2 \sim \left(k_h \left|\overline{U} - c\right|\hat{\delta}\right)^2. \tag{3}$$

For calculating the subgrid-scale vertical velocity variances, we also adopted Lyu et al.'s (2023) modification of setting the horizontal wavelength to 10 km as a scaling factor, as well as their approach for implementing the wave-induced vertical velocity variance in the second version of the two-moment Morrison and Gettelman microphysics scheme (MG2; Gettelman et al., 2010, 2019; Gettelman & Morrison, 2015).

The wave-induced (a) temperature perturbations and (b) vertical velocity variances are estimated individually for each gravity wave source (orographic, convective, and frontal). The perturbation with the largest amplitude is then selected at each grid point to represent the peak amplitude of temperature fluctuations $\left(\left|\hat{T}\right|\right)$ and total wave-induced vertical velocity variances. We note that the different types of gravity wave perturbations from each wave source can be used together or separately, by specifying the corresponding CESM namelist variables. The wave-induced fluctuations are limited to inputs for the chemistry module and the MG2 microphysics scheme but are not incorporated into the model's resolved dynamical fields.

2.4. Sub-Stepping Method and Stochastic Approach

Using information about the temperature fluctuations, we applied the sub-stepping method to the chemistry module as follows: the time evolution of temperature fluctuation is assumed to have a form of sine wave with an estimated amplitude of $\left|\hat{T}\right|$ and a period of one model time step (30 min); the temperature for the chemistry is sampled at 10 intermediate sub-time steps (every 3 min); and the chemistry and associated processes are updated with the changing temperature at each sub-time step to represent the changes in multiple chemical species as the wave-induced temperature fluctuations evolve. The limitation of choosing 30 min as the wave intrinsic period was discussed in Weimer et al. (2023), and a 30-min wave period could be reasonable under limited conditions (e.g., strong background wind conditions for mesoscale gravity waves, such as those in the polar vortex).

Weimer et al. (2023) have developed an alternative way of simulating wave-driven temperature perturbations other than the sub-stepping method: a stochastic approach using sine-wave-distributed random $\left|\hat{T}\right|$. In the stochastic approach, the phase of the wave is chosen as a random variable between $-\pi/2$ and $\pi/2$ to simulate various phases of gravity waves at each model time step (for details, see Section 2 in Weimer et al., 2023). Stochastically selecting $\left|\hat{T}\right|$ at each model time step (30 min) is equivalent to assuming that the intrinsic period of the wave is equal to or greater than 30 min. Since the stochastic approach does not involve any sub-stepping, it can reduce computational costs while reproducing similar results compared to the sub-stepping method in long-term statistics. In this study, we confine the analysis to the sub-stepping method to assess changes in chemistry occurring over a time scale of a few hours; however, the stochastic approach is also available as an alternative option for future studies. For example, it can be used to examine the influence of different initial phases of wave-induced perturbations on chemical species at the model's dynamical time step.

2.5. Experiments

We ran two sets of historical experiments, one implementing the sub-grid scale non-orographic gravity wave perturbations on the chemistry through sub-stepping (GW), and another reference simulation without the sub-grid scale wave parameterizations (REF). To highlight the influence of non-orographic gravity waves, we set the scaling factor for temperature perturbations induced by orographic waves to zero in the GW runs. However, as mentioned in an earlier section, temperature perturbations from different types of wave sources can be used

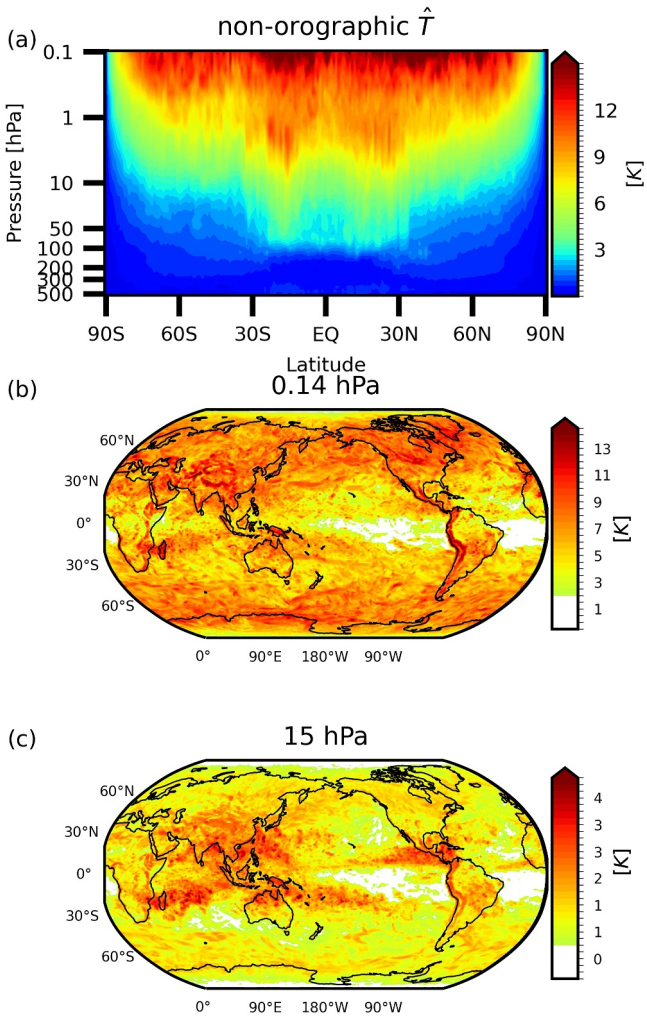

Figure 1. Maximum values of daily mean $\hat{T}$ in 2007 for the "non-orographic gravity wave" (GW) runs. The results displayed are the maximum value of all grid points as a function of latitude (top), maximum value at each grid point at the 0.14 hPa level (middle), and 15 hPa level (bottom).

together or separately, depending on the research focus. We chose to analyze the year 2007, following Weimer et al. (2023). The sub-stepping is also applied in the REF simulation but without temperature fluctuations in order to maintain consistency with the GW simulation by accounting for any variability that may be due to the sub-stepping process itself. The chemistry responses to sub-grid scale gravity wave parameterizations are dependent on internal climate variability. Here we use 5 ensemble members for each set of experiments, run with slightly different initial dates ranging from 15 December 2006 to 23 December 2006 with 2 days interval, to isolate the signatures of gravity waves from other forms of internal climate variability. All ensemble members were integrated until 31 December 2007.

We also run another experiment (MG2-GW) applying wave-induced vertical velocity fluctuations to the MG2 scheme, following Lyu et al. (2023). In the MG2-GW runs, configurations other than the vertical velocity fluctuations were identical to the REF runs (i.e., the temperature perturbations were set to zero) to highlight the difference arising from the vertical variance perturbations only. The MG2-GW runs were integrated for 4 months, from 1 January 2007, to 30 April 2007, as we focus on demonstrating any changes occurring on a seasonally averaged time scale.

3. Results

We present the global distribution of gravity wave-induced temperature perturbations, $\hat{T}$, in Figure 1. We first consider the maximum value of daily mean $\hat{T}$ from all five ensemble members of the GW simulation. The amplitude of temperature fluctuations increases with height at all latitudes, as atmospheric density decreases (Figure 1a). Temperature fluctuations are pronounced over the extratropical latitudes, with large amplitudes of approximately 15 K estimated at 0.14 hPa level. These temperature fluctuation patterns over the extratropics indicate significant contributions by waves generated from frontal systems (Figure 1b; Figures S2a–S2c in Supporting Information S1). At the tropical latitudes, temperature perturbations are particularly pronounced over the western Pacific warm pool region as well as the eastern equatorial Pacific, reaching maximum amplitudes of ∼5 K at 15 hPa level. This suggests a major influence of waves generated by convective heating sources (Figure 1c; Figures S2d–S2f in Supporting Information S1). While non-orographic gravity waves exhibit some features over the mountains (likely amplified due to significant orographic precipitation biases in CESM, as reported in previous studies; Sakaguchi et al., 2018; Reboita et al., 2024), they also exhibit pronounced signatures over the tropical latitudes and over the ocean (Figure 1), where the influences of orographic waves were limited or zero (see Figures 2 and 7 in Weimer et al., 2023). Thus, the results in Figure 1 suggest that non-orographic waves need to be accounted for to achieve a more realistic representation of the wave-induced temperature variability.

The results presented here are based on temperature fluctuations internally generated by the model, without any additional scaling applied to compare with observations. This is because the amplitudes of temperature fluctuations induced by non-orographic waves are poorly constrained quantities on a global scale, as it is challenging to distinguish non-orographic from orographic wave influences in observations. Thus, in practice, the amplitudes of fluctuations can be considered as parameters that can be tuned to the extent observations are available. We note that new data sets, based on observations from satellites and superpressure balloons, have recently become available, offering comprehensive statistics on temperature fluctuations associated with both orographic and non-orographic gravity waves (Bramberger et al., 2022; Corcos et al., 2021; Ern et al., 2018; Hindley et al., 2020). Future investigations could include comparisons with observations using both orographic and non-orographic parameterizations.

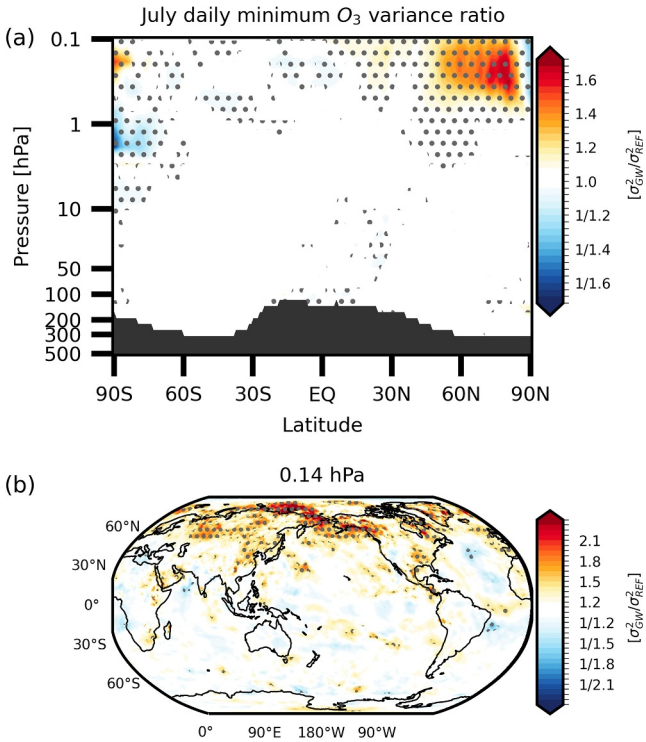

Figure 2. Ratio of the variance in daily minimum ozone concentration between GW and REF runs. The results displayed are the daily minimum values in all grid points as a function of latitude (top) and values at each grid point at the 0.14 hPa level (bottom) in July 2007. Note the non-linear color scale in both panels. Regions within the troposphere are masked out in the upper panel. Stippling indicates regions where the ratios exceed the 95% threshold.

We next explore the influences of gravity waves on middle atmosphere chemistry, particularly focusing on ozone concentrations, which are known to be strongly sensitive to temperature in the upper stratosphere and lower mesosphere (Barnett et al., 1975; Brasseur & Solomon, 2005; Prather, 1981). Figure 2 reveals ratios of variance in daily minimum ozone concentrations between the GW and REF runs. The daily minimum ozone value reflects the lowest instantaneous ozone concentration occurring at the sub-stepping time scale (3 min). All available time steps based on five ensemble members from each simulation are used to calculate the variances; thus, the variances are estimated over 5 ensemble members X 31 days X 288 longitudinal grid points = 44,640 samples for Figure 2a, and over 165 samples (5 ensemble members X 31 days) for Figure 2b. The F statistic is used to assess the statistical significance of the ratios between variances ($p < 0.05$). The seasonal cycle was not removed in order to highlight regions where changes in variability due to waves exceed the amplitudes of variation following the seasonal cycle during the analysis period. We analyze July 2007, but the results are not sensitive to a specific period as similar results were found from August to October of the same year (not shown).

We focus on the daily minimum ozone concentration for the following reasons. Observational and modeling studies have shown that the diurnal cycle of ozone above ~1 hPa is characterized by substantially smaller daytime ozone concentrations compared to nighttime concentrations (Haefele et al., 2008; Huang et al., 2008, 2014; Lean, 1982; Sakazaki et al., 2013; Schanz et al., 2014). This is because the ozone distribution in that region can be described by ozone photochemistry in a pure oxygen atmosphere (i.e., the Chapman mechanism), where the daytime ozone concentration is smaller than the nighttime concentration due to photolysis by UV light (Brasseur & Solomon, 2005; Chapman, 1930; Prather, 1981). Some photochemical reactions in the Chapman mechanism (e.g., the recombination of atomic oxygen and ozone), which are highly temperature-sensitive, occur primarily during the daytime. Thus, to investigate the influence of gravity waves on ozone variability, we focus on minimum ozone concentration during daytime and its sensitivity to the wave-induced temperature variations.

The key result in Figure 2a is that the non-orographic gravity waves increase the variability of daily minimum ozone concentrations in the lower mesosphere between ~0.3 hPa and 0.07 hPa around 60°N. In Figure 2b, we focus on a single pressure level (0.14 hPa) to exclude the influences of the variances arising from the longitudinally asymmetric component of the ozone distribution. At the 0.14 hPa level, local variances of daily minimum ozone increase by a factor of up to ~2 over the North Pacific (Figure 2b).

We further explore the connection between changes in chemistry and gravity wave temperature fluctuations. Figure 3 exhibits the time series of daily minimum ozone concentration, daily mean wave-induced temperature fluctuations, and daily mean temperature, focusing on a specific grid point representing a hot spot of frontal gravity wave activity near the North Pacific. Figure 3a reveals an average decrease of roughly ~13 ppbv in the daily minimum ozone concentration in the GW runs compared to the REF runs during the first 10 days of July. The difference in minimum ozone concentrations between the GW and REF runs (i.e., difference between red and blue lines) in early July is also larger than the internal variability among different ensembles (i.e., the red or blue shading).

More importantly, substantial increases in sub-grid scale temperature fluctuations are also shown over the periods that correspond to significant differences in the minimum ozone concentrations in the two experiments (Figures 3a and 3b). The amplitudes of $\hat{T}$ (>~5 K) are larger than changes due to the internal variability of daily mean temperature, and thus can have some local effects on strongly temperature dependent chemical reactions. Larger decreases in minimum ozone concentration are revealed in the sensitivity experiments run with larger amplitudes of temperature perturbations (with scaling factor = $\sqrt{3}$; Figure S3 in Supporting Information S1), further suggesting a causal relationship between them. In the following section, we explore the influences of waves on the ozone concentration and chemical reactions exhibiting temperature dependency.

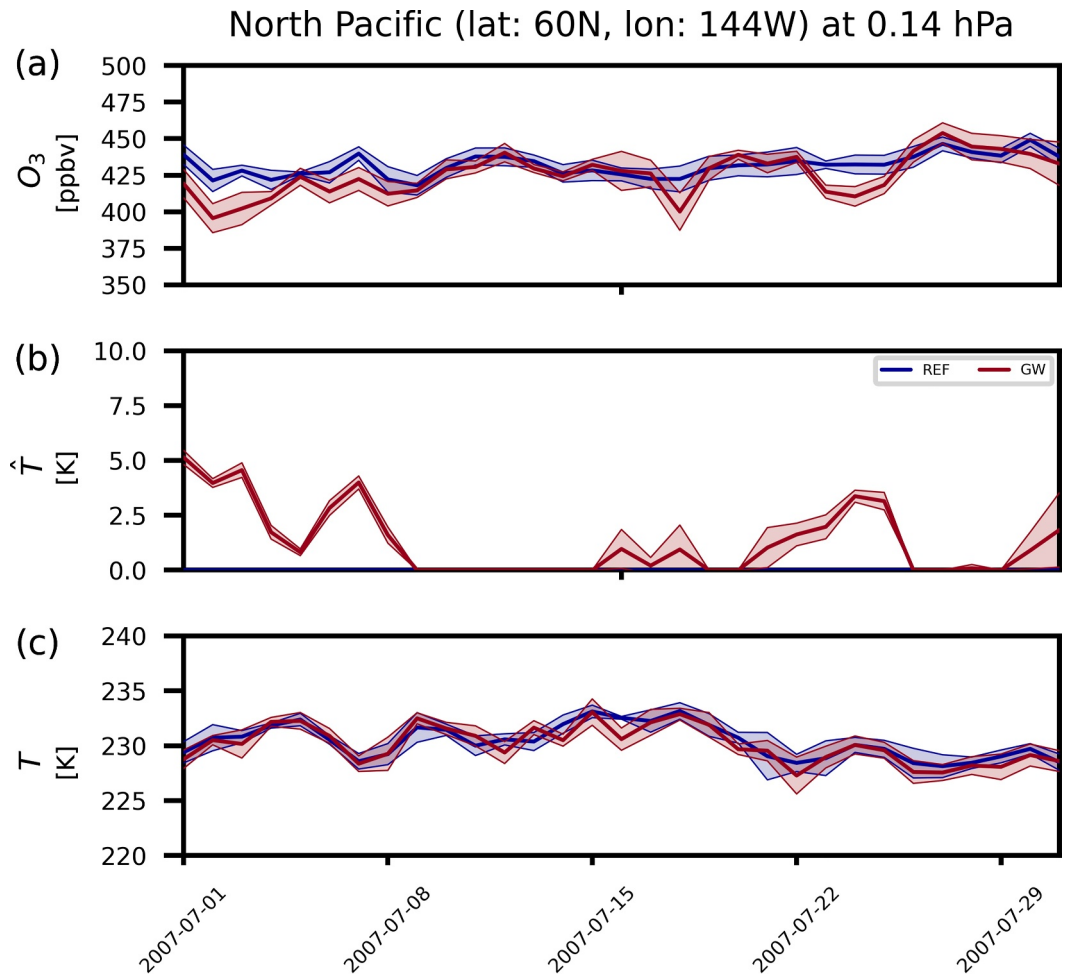

Figure 3. Timeseries of daily minimum concentration of ozone (top), daily mean wave-induced temperature perturbation (middle), and daily mean temperature (bottom) at a single WACCM grid point over the North Pacific (144°W, 60°N) at 0.14 hPa level. Each colored line and range represents the results based on the ensemble mean and spread of the (red) GW and (blue) REF runs. The spread is defined as one standard deviation among ensemble members for each field on each day.

Figure 4 presents timeseries of ozone concentration, wave-induced temperature fluctuations, and reaction rates that drive ozone chemistry at the same location over the North Pacific as in Figure 3 but focusing on 2-hr intervals around the time when the daily minimum ozone occurs. The results in Figure 4 are based on an additional experiment run with the same configuration as in the GW runs, but the integration was started from 21 June 2007, and the variables were outputted at a higher frequency (3-min intervals) to investigate the influences of waves on the fluctuations in ozone concentration.

Black dots in Figure 4a indicate instantaneous ozone mixing ratio outputted at each sub-time step. The ozone mixing ratio shows a nearly sinusoidal oscillation with a period of 30 min (which is equal to one sub-stepping cycle and the WACCM dynamical time step) and a peak-to-peak amplitude of ∼60 ppbv on 2 July 2007 (Figure 4a). This oscillation in ozone concentration is shown only in the GW runs, not in the REF runs (Figure S4a in Supporting Information S1), which in turn leads to increases in the daytime ozone variability in the GW runs, compared to variability in the REF runs (Figure 3a and Figure S4a in Supporting Information S1). It is noteworthy that satellite measurements with sufficient temporal and horizontal resolution may be able to sample variations in ozone comparable to these chemical changes over the wave-induced fluctuations.

Ozone concentrations (Figure 4a) and temperature perturbations (Figure 4b) are anti-correlated with each other. To assess the cause of the relationship between the ozone concentration and temperature, we first identify the chemical reactions that are primary drivers of the ozone variations, and then explore their temperature

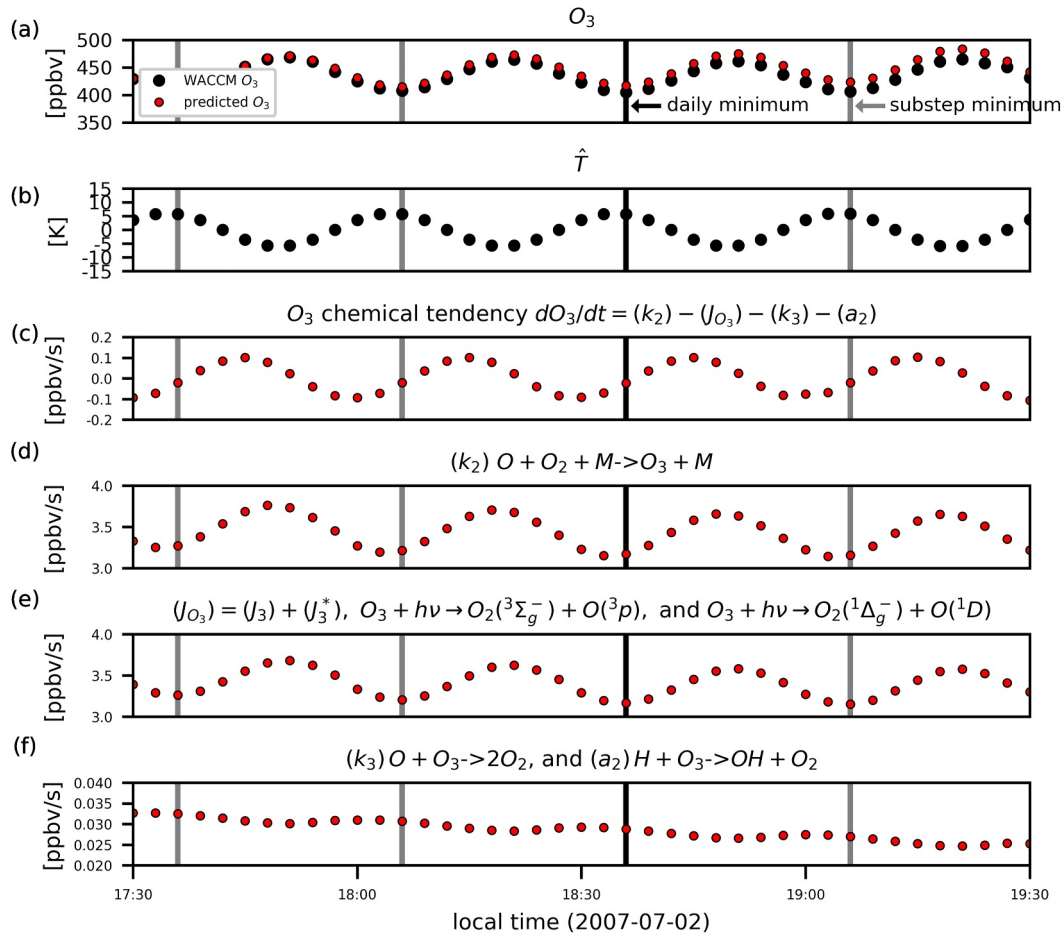

Figure 4. Timeseries of daytime (a) ozone concentration, (b) wave-induced temperature perturbation, (c) net chemical rate for ozone, (d) three-body recombination reaction rate, (e) ozone photolysis rate (the sum of two indicated pathways producing O^3P and O^1D, respectively), and (f) atomic oxygen-ozone recombination rate and ozone-hydrogen reaction rate. Black dots in panel (a) indicate the instantaneous ozone mixing ratio, while red dots represent the corresponding values estimated based on the sum of chemical rates in rows (d–f). All results are instantaneous values sampled at 3-min intervals. The timing for the absolute daily minimum ozone is indicated by black shading and timings for relative minimum values in each sub-step cycle are marked by gray shading. All reaction rate coefficients, k_i, and photolysis rates, J_i, followed the notation used by Brasseur and Solomon (2005). The results are derived from the same location over the North Pacific as in Figure 3.

dependencies. Red dots in Figure 4c represent ozone's chemical tendency estimated as a sum of the three-body recombination reaction rate (Figure 4d), ozone's photolysis rate (Figure 4e), atomic oxygen-ozone recombination rate and ozone-hydrogen reaction rate (Figure 4f). These processes in Figures 4d–4f are known to be the dominant ozone sources and sinks in the lower mesosphere (Brasseur & Solomon, 2005).

Red dots in Figure 4a are shown to compare the ozone concentration calculated by the time integration of the net chemical tendency mentioned above (Figure 4c), with the actual ozone concentration time series (black dots in Figure 4a). Again, the ozone's chemical tendency is estimated as the sum of the chemical rates shown in Figures 4d–4f. The integration starts from the initial ozone concentration at local time 17:30 to avoid potential long-term drift due to dynamical transport and chemical losses from reactions not included in the calculation. We note that the absence of dynamical tendency (green dots in Figures S4e–S4f in Supporting Information S1) and chemical losses from other reactions (red dots in Figures S4e–S4f in Supporting Information S1) can accumulate errors in the predicted ozone concentration when integrated over time (Figure S4d in Supporting Information S1). However, we consider these errors are negligible in our 30-min analysis interval (i.e., within a sub-stepping cycle).

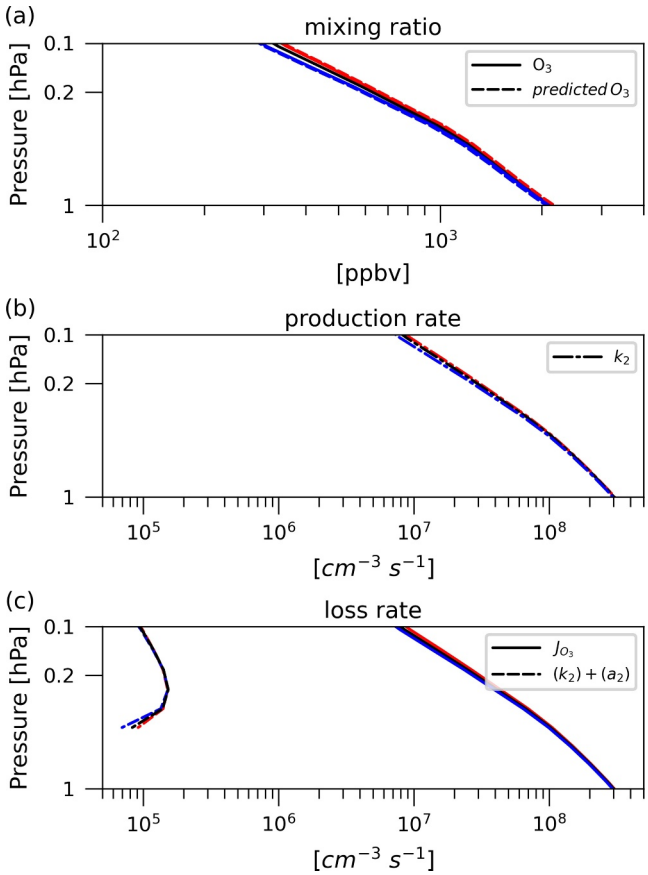

Figure 5. Vertical profile of ozone's (a) mixing ratio, (b) production rate, and (c) loss rate during a sub-stepping cycle between local time 18:00–19:00. The results are derived from the same location over the North Pacific as in Figures 3 and 4. The red, black, and blue lines represent values corresponding to the maximum, zero, and minimum displacement phase, respectively. The dashed-dotted line in panel (b) shows the three-body recombination rate, the solid line in panel (c) exhibits the photolysis rate, and the dashed line in panel (c) exhibits the sum of atomic oxygen-ozone recombination rate and ozone-hydrogen reaction rate. Dashed lines in panel (a) show predicted ozone abundances based on the net chemical rates defined as the sum of the three processes.

What are the main drivers of the simulated ozone variations? Close similarity between red and black dots in Figure 4a highlights that the calculation based on the net chemical rate captures most of the simulated ozone variations. Thus, the results in Figure 4a confirm that changes in ozone concentration are largely driven by the processes listed in Figures 4d–4f, with the three-body recombination reaction (Figure 4d) and photolysis (Figure 4e) respectively being the main source and sink of ozone at this location given their large amplitudes.

We now explore the temperature dependencies of the photochemical reactions in Figures 4d–4f. Both the rates of ozone production (Figure 4d) and the photolysis (Figure 4e) display distinct oscillatory pattern as well as an out-of-phase relationship with the temperature perturbation (Figures 4b, 4d, and 4e). This temperature dependencies of ozone reaction rates are due to the combined effects of (a) the temperature dependency of reaction rate coefficients and (b) the temperature induced air density variations, following the ideal gas law (Brasseur & Solomon, 2005; Chapman, 1930; Lean, 1982; Prather, 1981). The temperature dependencies of ozone photochemistry (Figures 4d–4f), in turn, lead to oscillatory behavior in the net ozone tendency (Figure 4c), as the net changes in ozone are governed by a balance between these processes. Together, the results in Figure 4 reveal that the gravity wave-induced temperature perturbations (a) cause the sinusoidal oscillation in the ozone mixing ratio, and (b) lead to increases in the daytime ozone variability in the GW runs compared to the variability in the REF runs.

Figure 5 exhibits the vertical structure of changes in ozone mixing ratio (Figure 5a), production rate (Figure 5b), and loss rate (Figure 5c) during a sub-stepping cycle between local time 18:30–19:00 between 1 and 0.05 hPa. The red, black, and blue lines represent values corresponding to the maximum, zero, and minimum during a cycle of the wave, respectively. Large variations in the ozone mixing ratio and chemical rates are obtained above the ∼0.2 hPa level. The results here indicate that the increase in daily minimum ozone in the GW runs shown in Figure 2 is primarily due to the wave-induced temperature fluctuations that affect the temperature-dependent chemical rates involved in ozone chemistry, which in turn lead to increases in daily ozone variability. Together, the results in Figures 2–5 demonstrate an example of many instantaneous processes associated with sub-grid scale gravity wave activity that were not simulated in the standard version of WACCM simulations. This highlights the role of sub-grid scale waves on atmospheric chemistry.

The role of non-orographic gravity waves in cirrus cloud formation is briefly summarized in Figure 6 as another implication of gravity wave perturbations in climate modeling. In WACCM6, the MG2 scheme predicts ice nucleation in cirrus cloud formation using sub-grid vertical velocity variances. In the default setting, the vertical velocity variances are associated with the amplitudes of sub-grid scale turbulent motion derived from CLUBB (Cloud Layers Unified by Binormals; Golaz et al., 2002a, 2002b). Here, we also estimated sub-grid vertical velocity variances associated with convective and frontal gravity waves and introduced them into the ice nucleation parameterization.

Figures 6a, 6c, and 6e compare the sub-grid scale vertical velocity variances for the ice nucleation parameterization between the MG2-GW and REF simulations. Both runs show high values of the vertical velocity variances over tropical latitudes, consistent with a previous study based on 7-km high-resolution modeling (Barahona et al., 2017). Vertical velocity variances are increased in the upper troposphere over the tropical and extratropical latitudes (60°S–60°N) with inclusion of the wave-induced vertical velocity fluctuations (Figure 6e). As expected, cloud ice mixing ratio also increases in the same regions (Figure 6f), suggesting that the onset of ice supersaturation is triggered by the sub-grid scale gravity waves. Our results highlight that the influence of non-orographic waves is pronounced over tropical and extratropical latitudes in the upper troposphere. This finding is consistent

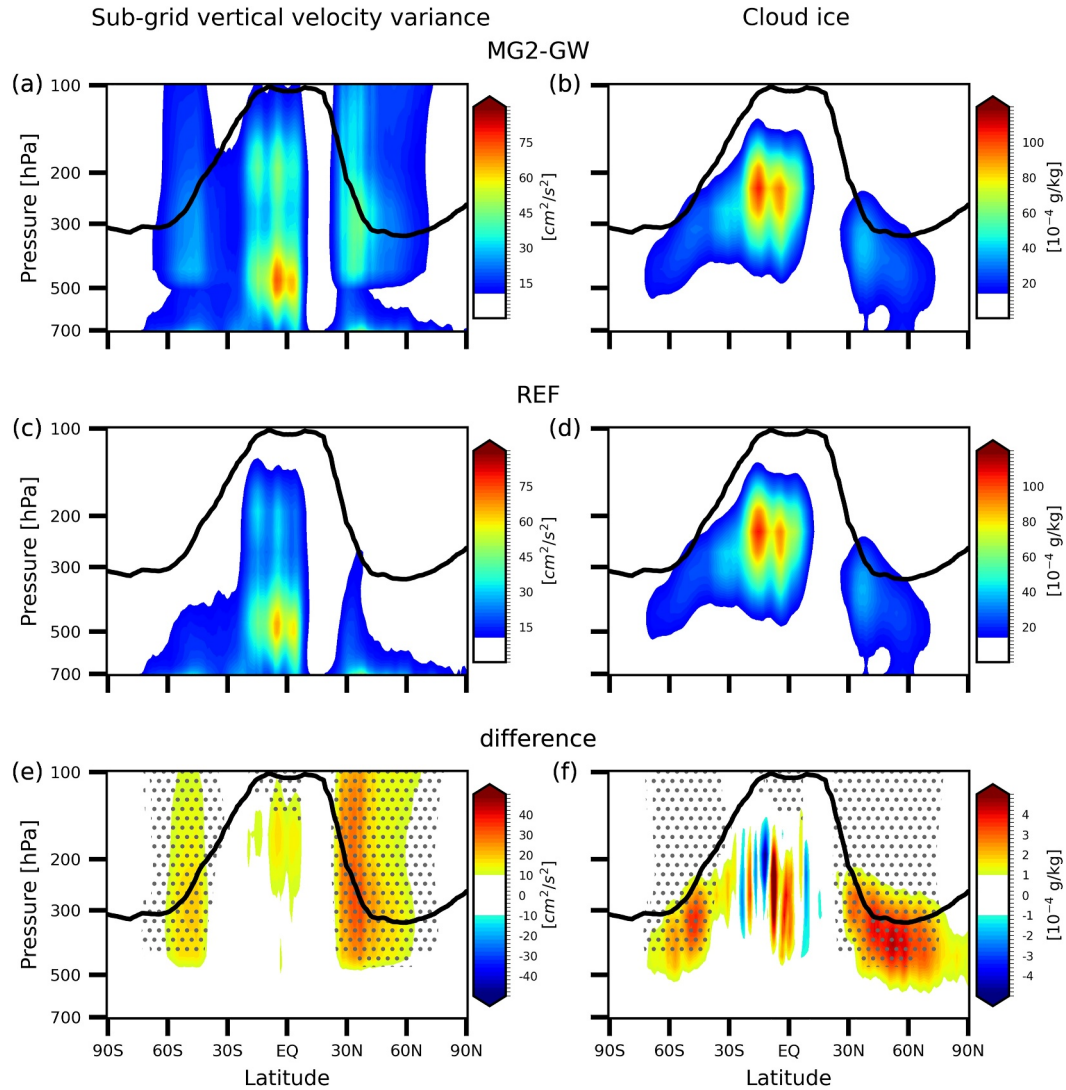

Figure 6. Zonal mean distribution of (left) sub-grid scale vertical velocity variance for ice formation (cm s^{-1}), and (right) grid-box cloud ice amount (kg kg^{-1}) from (top) MG2-GW, (middle) REF, and (bottom) difference between MG2-GW and REF simulations. The results are averaged over January–March. Stippling indicates regions where the relative error with respect to the REF runs exceeds 100%.

with a previous study based on observational analyses and trajectory modeling (Schoeberl et al., 2016), which found that gravity waves increase the upper tropical tropopause cloud fraction. Another study based on numerical simulations using balloon-observed temperature data (Dinh et al., 2016) also suggests that high-frequency temperature fluctuations due to gravity waves can control the homogeneous nucleation of cloud ice in the vicinity of the tropical tropopause.

We find that the main results presented here (scaling factor = 1; Figures 2, 3, and 6) remain qualitatively similar to results from the sensitivity experiments run with larger amplitudes of wave-induced perturbations (scaling factor = $\sqrt{3}$; Figures S3, S5, and S6 in Supporting Information S1).

4. Summary and Conclusions

Recent modeling studies introduced a method to account for the effects of subgrid-scale *orographic* gravity-wave-induced dynamical perturbations in community climate models: (a) temperature perturbations on the

atmospheric chemistry in WACCM6 (Weimer et al., 2023), and (b) vertical velocity perturbations on cirrus cloud formations in CAM6 (Lyu et al., 2023). The methods estimate the dynamical perturbations of gravity waves based on the model's gravity wave parameterizations and introduce them into the chemistry module and microphysics scheme (respectively). Here we extended the method to also include perturbations by *non-orographic* gravity waves arising from frontal activity and convection. The sub-grid scale temperature fluctuations are estimated in a similar manner to the method outlined in Weimer et al. (2023), except that the momentum fluxes were calculated based on a wave spectrum instead of a monochromatic wave. We integrated momentum fluxes over a phase speed spectrum to estimate the total wave momentum flux from different wavenumbers and used the results to calculate peak wave displacement amplitudes. The wave-induced fluctuations were then applied to chemistry as a sine-wave perturbation using a time interval sub-stepping method. Similarly, sub-grid vertical velocity perturbations were derived following the method by Lyu et al. (2023), and then applied to the MG2 scheme for the ice nucleation parameterization.

Two sets of 1-year long simulations were conducted with WACCM6: one based on the default WACCM6, and a second one with the sub-grid scale gravity wave perturbations. We compared the simulation in the two experiments to assess the global pattern of temperature fluctuations induced by non-orographic waves, as well as the role of wave-induced dynamical perturbations on an example case of middle atmosphere chemistry and cirrus cloud formation in the upper troposphere. The key implications of the method are as follows.

1. The non-orographic gravity waves increase the variability of chemical reaction rates, particularly in the upper stratosphere and lower mesosphere, which, in turn, leads to an increase in the daytime variability of the ozone concentration.
2. The non-orographic waves also enhance homogeneous nucleation and thus increase cirrus clouds in the upper troposphere across tropical to extratropical latitudes.

Our method provides estimates of the amplitudes of the temperature perturbations based on WACCM's internal physics and parameterizations. This has various possible implications for climate and chemistry. Convective gravity waves are known to play an important role in the cold point tropopause temperature as well as stratospheric water vapor abundances (Jensen & Pfister, 2004; Kim & Alexander, 2013, 2015). While beyond the scope of the current work, our method could be used to address the effects of sub-grid scale gravity waves on the variability of simulated cold point temperatures. Future work could also compare the detailed statistics of simulated wave-induced temperature fluctuations, such as amplitudes, frequencies, and spatial patterns, with the characteristics of observed gravity waves on a global scale.

Data Availability Statement

The data set used in the generation of the figures of this paper are available at (Yook, 2024). The model code modifications to add the parameterization to the published version of CESM2.1.4 (see Danabasoglu et al., 2020) can also be found at Yook (2024).

Acknowledgments
S. S and S. Y. are supported by grant AGS-1906719 from the Atmospheric Chemistry Division of the U.S. National Science Foundation (NSF). The CESM project is supported by the NSF and the Office of Science (BER) of the U.S. Department of Energy (DOE). The authors acknowledge the Climate Simulation Laboratory at NCAR's Computational and Information Systems Laboratory (CISL; sponsored by NSF and other agencies) for providing computing and storage resources that have contributed to the research results reported within this paper. The authors thank Petr Šácha and two anonymous reviewers for their helpful comments on the manuscript.

References

Alexander, M. J., Geller, M., McLandress, C., Polavarapu, S., Preusse, P., Sassi, F., et al. (2010). Recent developments in gravity-wave effects in climate models and the global distribution of gravity-wave momentum flux from observations and models. *Quarterly Journal of the Royal Meteorological Society*, *136*(650), 1103–1124. https://doi.org/10.1002/qj.637

Alexander, M. J., Liu, C. C., Bacmeister, J., Bramberger, M., Hertzog, A., & Richter, J. H. (2021). Observational validation of parameterized gravity waves from tropical convection in the Whole Atmosphere Community Climate Model. *Journal of Geophysical Research: Atmospheres*, *126*(7), e2020JD033954. https://doi.org/10.1029/2020jd033954

Alexander, M. J., & Ortland, D. A. (2010). Equatorial waves in high resolution dynamics limb sounder (HIRDLS) data. *Journal of Geophysical Research*, *115*(D24), D24111. https://doi.org/10.1029/2010jd014782

Alpert, J. C. (2004). Sub-grid scale mountain blocking at NCEP. *Proceedings of 20th Conference on WAF, 16th conference on NWP, Citeseer*.

Andrews, D. G., Holton, J. R., & Leovy, C. B. (1987). *Middle atmosphere dynamics*. Academic Press.

Barahona, D., Molod, A., & Kalesse, H. (2017). Direct estimation of the global distribution of vertical velocity within cirrus clouds. *Scientific Reports*, *7*(1), 6840. https://doi.org/10.1038/s41598-017-07038-6

Barnett, J., Houghton, J., & Pyle, J. (1975). The temperature dependence of the ozone concentration near the stratopause. *Quarterly Journal of the Royal Meteorological Society*, *101*(428), 245–257. https://doi.org/10.1256/smsqj.42807

Beres, J. H., Alexander, M. J., & Holton, J. R. (2004). A method of specifying the gravity wave spectrum above convection based on latent heating properties and background wind. *Journal of the Atmospheric Sciences*, *61*(3), 324–337. https://doi.org/10.1175/1520-0469(2004)061<0324:amostg>2.0.co;2

Beres, J. H., Garcia, R. R., Boville, B. A., & Sassi, F. (2005). Implementation of a gravity wave source spectrum parameterization dependent on the properties of convection in the Whole Atmosphere Community Climate Model (WACCM). *Journal of Geophysical Research*, *110*(D10), D10108. https://doi.org/10.1029/2004jd005504

Borrmann, S., Solomon, S., Dye, J. E., Baumgardner, D., Kelly, K. K., & Chan, K. R. (1997). Heterogeneous reactions on stratospheric background aerosols, volcanic sulfuric acid droplets, and type I polar stratospheric clouds: Effects of temperature fluctuations and differences in particle phase. *Journal of Geophysical Research*, *102*(D3), 3639–3648. https://doi.org/10.1029/96jd02976

Bramberger, M., Alexander, M. J., Davis, S., Podglajen, A., Hertzog, A., Kalnajs, L., et al. (2022). First super-pressure balloon-borne fine-vertical-scale profiles in the upper TTL: Impacts of atmospheric waves on cirrus clouds and the QBO. *Geophysical Research Letters*, *49*(5), e2021GL097596. https://doi.org/10.1029/2021gl097596

Brasseur, G. P., & Solomon, S. (2005). Composition and chemistry. *Aeronomy of the Middle Atmosphere: Chemistry and Physics of the Stratosphere and Mesosphere*, 265–442.

Bushell, A. C., Butchart, N., Derbyshire, S. H., Jackson, D. R., Shutts, G. J., Vosper, S. B., & Webster, S. (2015). Parameterized gravity wave momentum fluxes from sources related to convection and large-scale precipitation processes in a global atmosphere model. *Journal of the Atmospheric Sciences*, *72*(11), 4349–4371. https://doi.org/10.1175/jas-d-15-0022.1

Carslaw, K., Luo, B., Clegg, S., Peter, T., Brimblecombe, P., & Crutzen, P. (1994). Stratospheric aerosol growth and HNO3 gas phase depletion from coupled HNO3 and water uptake by liquid particles. *Geophysical Research Letters*, *21*(23), 2479–2482. https://doi.org/10.1029/94gl02799

Carslaw, K. S., Wirth, M., Tsias, A., Luo, B. P., Dörnbrack, A., Leutbecher, M., et al. (1998a). Particle microphysics and chemistry in remotely observed mountain polar stratospheric clouds. *Journal of Geophysical Research*, *103*(D5), 5785–5796. https://doi.org/10.1029/97jd03626

Carslaw, K. S., Wirth, M., Tsias, A., Luo, B. P., Dörnbrack, A., Leutbecher, M., et al. (1998b). Increased stratospheric ozone depletion due to mountain-induced atmospheric waves. *Nature*, *391*(6668), 675–678. https://doi.org/10.1038/35589

Chapman, S. (1930). XXXV. On ozone and atomic oxygen in the upper atmosphere. *The London, Edinburgh and Dublin Philosophical Magazine and Journal of Science*, *10*(64), 369–383. https://doi.org/10.1080/14786443009461588

Charron, M., & Manzini, E. (2002). Gravity waves from fronts: Parameterization and middle atmosphere response in a general circulation model. *Journal of the Atmospheric Sciences*, *59*(5), 923–941. https://doi.org/10.1175/1520-0469(2002)059<0923:gwffpa>2.0.co;2

Chun, H. Y., & Kim, Y. H. (2008). Secondary waves generated by breaking of convective gravity waves in the mesosphere and their influence in the wave momentum flux. *Journal of Geophysical Research*, *113*(D23), D23107. https://doi.org/10.1029/2008jd009792

Corcos, M., Hertzog, A., Plougonven, R., & Podglajen, A. (2021). Observation of gravity waves at the tropical tropopause using superpressure balloons. *Journal of Geophysical Research: Atmospheres*, *126*(15), e2021JD035165. https://doi.org/10.1029/2021jd035165

Danabasoglu, G., Lamarque, J. F., Bacmeister, J., Bailey, D. A., DuVivier, A. K., Edwards, J., et al. (2020). The community earth system model version 2 (CESM2). *Journal of Advances in Modeling Earth Systems*, *12*, e2019MS001916. https://doi.org/10.1029/2019ms001916

Davis, N. A., Callaghan, P., Simpson, I. R., & Tilmes, S. (2022). Specified dynamics scheme impacts on wave-mean flow dynamics, convection, and tracer transport in CESM2 (WACCM6). *Atmospheric Chemistry and Physics*, *22*(1), 197–214. https://doi.org/10.5194/acp-22-197-2022

Dean, S., Flowerdew, J., Lawrence, B., & Eckermann, S. (2007). Parameterisation of orographic cloud dynamics in a GCM. *Climate Dynamics*, *28*(6), 581–597. https://doi.org/10.1007/s00382-006-0202-0

Dewan, E. Á., Picard, R. H., O'Neil, R. R., Gardiner, H. A., Gibson, J., Mill, J. D., et al. (1998). MSX satellite observations of thunderstorm-generated gravity waves in mid-wave infrared images of the upper stratosphere. *Geophysical Research Letters*, *25*(7), 939–942. https://doi.org/10.1029/98gl00640

Dinh, T., Podglajen, A., Hertzog, A., Legras, B., & Plougonven, R. (2016). Effect of gravity wave temperature fluctuations on homogeneous ice nucleation in the tropical tropopause layer. *Atmospheric Chemistry and Physics*, *16*(1), 35–46. https://doi.org/10.5194/acp-16-35-2016

Dörnbrack, A., Leutbecher, M., Kivi, R., & Kyrö, E. (1999). Mountain-wave-induced record low stratospheric temperatures above northern Scandinavia. *Tellus A: Dynamic Meteorology and Oceanography*, *51*(5), 951–963. https://doi.org/10.3402/tellusa.v51i5.14504

Emmons, L. K., Walters, S., Hess, P. G., Lamarque, J. F., Pfister, G. G., Fillmore, D., et al. (2010). Description and evaluation of the model for ozone and related chemical tracers, version 4 (MOZART-4). *Geoscientific Model Development*, *3*(1), 43–67. https://doi.org/10.5194/gmd-3-43-2010

Ern, M., Trinh, Q. T., Preusse, P., Gille, J. C., Mlynczak, M. G., Russell, J. M. III, & Riese, M. (2018). GRACILE: A comprehensive climatology of atmospheric gravity wave parameters based on satellite limb soundings. *Earth System Science Data*, *10*(2), 857–892. https://doi.org/10.5194/essd-10-857-2018

Fritts, D. C., & Alexander, M. J. (2003). Gravity wave dynamics and effects in the middle atmosphere. *Reviews of Geophysics*, *41*(1), 1003. https://doi.org/10.1029/2001rg000106

Fritts, D. C., & Nastrom, G. D. (1992). Sources of mesoscale variability of gravity waves. Part II: Frontal, convective, and jet stream excitation. *Journal of the Atmospheric Sciences*, *49*(2), 111–127. https://doi.org/10.1175/1520-0469(1992)049<0111:somvog>2.0.co;2

Garcia, R. R., & Solomon, S. (1985). The effect of breaking gravity waves on the dynamics and chemical composition of the mesosphere and lower thermosphere. *Journal of Geophysical Research*, *90*(D2), 3850–3868. https://doi.org/10.1029/jd090id02p03850

Gelaro, R., McCarty, W., Suárez, M. J., Todling, R., Molod, A., Takacs, L., et al. (2017). The modern-era retrospective analysis for research and applications, version 2 (MERRA-2). *Journal of Climate*, *30*(14), 5419–5454. https://doi.org/10.1175/jcli-d-16-0758.1

Gettelman, A., Liu, X., Ghan, S. J., Morrison, H., Park, S., Conley, A. J., et al. (2010). Global simulations of ice nucleation and ice supersaturation with an improved cloud scheme in the Community Atmosphere Model. *Journal of Geophysical Research*, *115*(D18), D18216. https://doi.org/10.1029/2009jd013797

Gettelman, A., Mills, M. J., Kinnison, D. E., Garcia, R. R., Smith, A. K., Marsh, D. R., et al. (2019). The whole atmosphere community climate model version 6 (WACCM6). *Journal of Geophysical Research: Atmospheres*, *124*(23), 12380–12403. https://doi.org/10.1029/2019jd030943

Gettelman, A., & Morrison, H. (2015). Advanced two-moment bulk microphysics for global models. Part I: Off-line tests and comparison with other schemes. *Journal of Climate*, *28*(3), 1268–1287. https://doi.org/10.1175/jcli-d-14-00102.1

Golaz, J.-C., Larson, V. E., & Cotton, W. R. (2002a). A PDF-based model for boundary layer clouds. Part I: Method and model description. *Journal of the Atmospheric Sciences*, *59*(24), 3540–3551. https://doi.org/10.1175/1520-0469(2002)059<3540:apbmfb>2.0.co;2

Golaz, J.-C., Larson, V. E., & Cotton, W. R. (2002b). A PDF-based model for boundary layer clouds. Part II: Model results. *Journal of the Atmospheric Sciences*, *59*(24), 3552–3571. https://doi.org/10.1175/1520-0469(2002)059<3552:apbmfb>2.0.co;2

Haefele, A., Hocke, K., Kämpfer, N., Keckhut, P., Marchand, M., Bekki, S., et al. (2008). Diurnal changes in middle atmospheric H2O and O3: Observations in the Alpine region and climate models. *Journal of Geophysical Research*, *113*(D17), D17303. https://doi.org/10.1029/2008jd009892

Hindley, N. P., Wright, C. J., Hoffmann, L., Moffat-Griffin, T., & Mitchell, N. J. (2020). An 18-year climatology of directional stratospheric gravity wave momentum flux from 3-D satellite observations. *Geophysical Research Letters*, *47*(22), e2020GL089557. https://doi.org/10.1029/2020gl089557

Holt, L. A., Alexander, M. J., Coy, L., Molod, A., Putman, W., & Pawson, S. (2016). Tropical waves and the quasi-biennial oscillation in a 7-km global climate simulation. *Journal of the Atmospheric Sciences*, *73*(9), 3771–3783. https://doi.org/10.1175/jas-d-15-0350.1

Holton, J. R. (1983). The influence of gravity wave breaking on the general circulation of the middle atmosphere. *Journal of the Atmospheric Sciences*, *40*(10), 2497–2507. https://doi.org/10.1175/1520-0469(1983)040<2497:tiogwb>2.0.co;2

Hoskins, B. J. (1982). The mathematical theory of frontogenesis. *Annual Review of Fluid Mechanics*, *14*(1), 131–151. https://doi.org/10.1146/annurev.fl.14.010182.001023

Huang, F., Mayr, H., Russell, J., III, & Mlynczak, M. (2014). Ozone and temperature decadal trends in the stratosphere, mesosphere and lower thermosphere, based on measurements from SABER on TIMED. In *Annales geophysicae*, (Vol. 32(8), pp. 935–949). Copernicus Publications. https://doi.org/10.5194/angeo-32-935-2014

Huang, F. T., Mayr, H. G., Russell, J. M. III, Mlynczak, M. G., & Reber, C. A. (2008). Ozone diurnal variations and mean profiles in the mesosphere, lower thermosphere, and stratosphere, based on measurements from SABER on TIMED. *Journal of Geophysical Research*, *113*(A4), A04307. https://doi.org/10.1029/2007ja012739

Jensen, E., & Pfister, L. (2004). Transport and freeze-drying in the tropical tropopause layer. *Journal of Geophysical Research*, *109*(D2), D02207. https://doi.org/10.1029/2003jd004022

Jensen, E. J., Toon, O. B., Pfister, L., & Selkirk, H. B. (1996). Dehydration of the upper troposphere and lower stratosphere by subvisible cirrus clouds near the tropical tropopause. *Geophysical Research Letters*, *23*(8), 825–828. https://doi.org/10.1029/96gl00722

Jewtoukoff, V., Hertzog, A., Plougonven, R., de la Camara, A., & Lott, F. (2015). Comparison of gravity waves in the Southern Hemisphere derived from balloon observations and the ECMWF analyses. *Journal of the Atmospheric Sciences*, *72*(9), 3449–3468. https://doi.org/10.1175/jas-d-14-0324.1

Jiang, J., Eckermann, S., Wu, D., Hocke, K., Wang, B., Ma, J., & Zhang, Y. (2005). Seasonal variation of gravity wave sources from satellite observation. *Advances in Space Research*, *35*(11), 1925–1932. https://doi.org/10.1016/j.asr.2005.01.099

Kärcher, B., & Ström, J. (2003). The roles of dynamical variability and aerosols in cirrus cloud formation. *Atmospheric Chemistry and Physics*, *3*, 823–838. https://doi.org/10.5194/acp-3-823-2003

Kim, J.-E., & Alexander, M. J. (2013). A new wave scheme for trajectory simulations of stratospheric water vapor. *Geophysical Research Letters*, *40*, 5286–5290. https://doi.org/10.1002/grl.50963

Kim, J. E., & Alexander, M. J. (2015). Direct impacts of waves on tropical cold point tropopause temperature. *Geophysical Research Letters*, *42*(5), 1584–1592. https://doi.org/10.1002/2014gl062737

Kim, Y. J., Eckermann, S. D., & Chun, H. Y. (2003). An overview of the past, present and future of gravity-wave drag parametrization for numerical climate and weather prediction models. *Atmosphere-Ocean*, *41*(1), 65–98. https://doi.org/10.3137/ao.410105

Kinnison, D., Brasseur, G. P., Walters, S., Garcia, R. R., Marsh, D. R., Sassi, F., et al. (2007). Sensitivity of chemical tracers to meteorological parameters in the MOZART-3 chemical transport model. *Journal of Geophysical Research*, *112*(D20), D20302. https://doi.org/10.1029/2006jd007879

Lean, J. L. (1982). Observation of the diurnal variation of atmospheric ozone. *Journal of Geophysical Research*, *87*(C7), 4973–4980. https://doi.org/10.1029/jc087ic07p04973

Lilly, D., & Kennedy, P. (1973). Observations of a stationary mountain wave and its associated momentum flux and energy dissipation. *Journal of the Atmospheric Sciences*, *30*(6), 1135–1152. https://doi.org/10.1175/1520-0469(1973)030<1135:ooasmw>2.0.co;2

Lindzen, R. S. (1981). Turbulence and stress owing to gravity wave and tidal breakdown. *Journal of Geophysical Research*, *86*(C10), 9707–9714. https://doi.org/10.1029/jc086ic10p09707

Lindzen, R. S., & Holton, J. R. (1968). A theory of the quasi-biennial oscillation. *Journal of the Atmospheric Sciences*, *25*(6), 1095–1107. https://doi.org/10.1175/1520-0469(1968)025<1095:atotqb>2.0.co;2

Lyu, K., Liu, X., Bacmeister, J., Zhao, X., Lin, L., Shi, Y., & Sourdeval, O. (2023). Orographic cirrus and its radiative forcing in NCAR CAM6. *Journal of Geophysical Research: Atmospheres*, *128*(10), e2022JD038164. https://doi.org/10.1029/2022jd038164

Marsh, D. R., Mills, M. J., Kinnison, D. E., Lamarque, J.-F., Calvo, N., & Polvani, L. M. (2013). Climate change from 1850 to 2005 simulated in CESM1 (WACCM). *Journal of Climate*, *26*(19), 7372–7391. https://doi.org/10.1175/jcli-d-12-00558.1

McFarlane, N. (1987). The effect of orographically excited gravity wave drag on the general circulation of the lower stratosphere and troposphere. *Journal of the Atmospheric Sciences*, *44*(14), 1775–1800. https://doi.org/10.1175/1520-0469(1987)044<1775:teooeg>2.0.co;2

McKenna, D., McKenna, D. S., Jones, R. L., Poole, L. R., Solomon, S., Fahey, D. W., et al. (1990). Calculations of ozone destruction during the 1988/89 Arctic winter. *Geophysical Research Letters*, *17*(4), 553–556. https://doi.org/10.1029/gl017i004p00553

Meilinger, S. K., Koop, T., Luo, B. P., Huthwelker, T., Carslaw, K. S., Krieger, U., et al. (1995). Size-dependent stratospheric droplet composition in lee wave temperature fluctuations and their potential role in PSC freezing. *Geophysical Research Letters*, *22*, 3031–3034. https://doi.org/10.1029/95gl03056

Miller, J. E. (1948). On the concept of frontogenesis. *Journal of the Atmospheric Sciences*, *5*(4), 169–171. https://doi.org/10.1175/1520-0469(1948)005<0169:otcof>2.0.co;2

Mills, M. J., Schmidt, A., Easter, R., Solomon, S., Kinnison, D. E., Ghan, S. J., et al. (2016). Global volcanic aerosol properties derived from emissions, 1990–2014, using CESM1 (WACCM). *Journal of Geophysical Research: Atmospheres*, *121*(5), 2332–2348. https://doi.org/10.1002/2015jd024290

Orr, A., Hosking, J. S., Delon, A., Hoffmann, L., Spang, R., Moffat-Griffin, T., et al. (2020). PSCs initiated by mountain waves in a global chemistry-climate model: A missing piece in fully modelling polar stratospheric ozone depletion. *Atmospheric Chemistry and Physics*, *20*, 1–15.

O'sullivan, D., & Dunkerton, T. J. (1995). Generation of inertia–gravity waves in a simulated life cycle of baroclinic instability. *Journal of the Atmospheric Sciences*, *52*, 3695–3716.

Penner, J. E., Zhou, C., Garnier, A., & Mitchell, D. L. (2018). Anthropogenic aerosol indirect effects in cirrus clouds. *Journal of Geophysical Research: Atmospheres*, *123*(20), 11652–11677. https://doi.org/10.1029/2018jd029204

Peter, T., Müller, R., Crutzen, P. J., & Deshler, T. (1994). The lifetime of leewave-induced ice particles in the Arctic stratosphere: II. Stabilization due to NAT-coating. *Geophysical Research Letters*, *21*(13), 1331–1334. https://doi.org/10.1029/93gl03019

Piani, C., Durran, D., Alexander, M., & Holton, J. (2000). A numerical study of three-dimensional gravity waves triggered by deep tropical convection and their role in the dynamics of the QBO. *Journal of the Atmospheric Sciences*, *57*(22), 3689–3702. https://doi.org/10.1175/1520-0469(2000)057<3689:ansotd>2.0.co;2

Potter, B. E., & Holton, J. R. (1995). The role of monsoon convection in the dehydration of the lower tropical stratosphere. *Journal of the Atmospheric Sciences*, *52*(8), 1034–1050. https://doi.org/10.1175/1520-0469(1995)052<1034:tromci>2.0.co;2

Prather, M. J. (1981). Ozone in the upper stratosphere and mesosphere. *Journal of Geophysical Research*, *86*(C6), 5325–5338. https://doi.org/10.1029/jc086ic06p05325

Reboita, M. S., de Souza Ferreira, G. W., Ribeiro, J. G. M., & Ali, S. (2024). Assessment of precipitation and near-surface temperature simulation by CMIP6 models in South America. *Environmental Research: Climate*, *3*(2), 025011. https://doi.org/10.1088/2752-5295/ad3fdb

Richter, J. H., Sassi, F., & Garcia, R. R. (2010). Toward a physically based gravity wave source parameterization in a general circulation model. *Journal of the Atmospheric Sciences*, *67*(1), 136–156. https://doi.org/10.1175/2009jas3112.1

Richter, J. H., Solomon, A., & Bacmeister, J. T. (2014). On the simulation of the quasi-biennial oscillation in the Community Atmosphere Model, version 5. *Journal of Geophysical Research: Atmospheres*, *119*(6), 3045–3062. https://doi.org/10.1002/2013jd021122

Sakaguchi, K., Leung, L. R., Burleyson, C. D., Xiao, H., & Wan, H. (2018). Role of troposphere-convection-land coupling in the southwestern Amazon precipitation bias of the Community Earth System Model version 1 (CESM1). *Journal of Geophysical Research: Atmospheres*, *123*(16), 8374–8399. https://doi.org/10.1029/2018jd028999

Sakazaki, T., Fujiwara, M., Mitsuda, C., Imai, K., Manago, N., Naito, Y., et al. (2013). Diurnal ozone variations in the stratosphere revealed in observations from the superconducting submillimeter-wave limb-emission sounder (SMILES) on board the international space station (ISS). *Journal of Geophysical Research: Atmospheres*, *118*(7), 2991–3006. https://doi.org/10.1002/jgrd.50220

Schanz, A., Hocke, K., & Kämpfer, N. (2014). Daily ozone cycle in the stratosphere: Global, regional and seasonal behaviour modelled with the whole atmosphere community climate model. *Atmospheric Chemistry and Physics*, *14*, 7645–7663. https://doi.org/10.5194/acp-14-7645-2014

Schoeberl, M., Dessler, A., Ye, H., Wang, T., Avery, M., & Jensen, E. (2016). The impact of gravity waves and cloud nucleation threshold on stratospheric water and tropical tropospheric cloud fraction. *Earth and Space Science*, *3*(8), 295–305. https://doi.org/10.1002/2016ea000180

Tabazadeh, A., Turco, R. P., & Jacobson, M. Z. (1994). A model for studying the composition and chemical effects of stratospheric aerosols. *Journal of Geophysical Research*, *99*(D6), 12897–12914. https://doi.org/10.1029/94jd00820

Tsias, A., Prenni, A., Carslaw, K., Onasch, T., Luo, B., Tolbert, M., & Peter, T. (1997). Freezing of polar stratospheric clouds in orographically induced strong warming events. *Geophysical Research Letters*, *24*(18), 2303–2306. https://doi.org/10.1029/97gl02181

Weimer, M., Buchmüller, J., Hoffmann, L., Kirner, O., Luo, B., Ruhnke, R., et al. (2021). Mountain-wave-induced polar stratospheric clouds and their representation in the global chemistry model ICON-ART. *Atmospheric Chemistry and Physics*, *21*(12), 9515–9543. https://doi.org/10.5194/acp-21-9515-2021

Weimer, M., Wilka, C., Kinnison, D. E., Garcia, R. R., Bacmeister, J. T., Alexander, M. J., et al. (2023). A method for estimating global subgrid-scale orographic gravity-wave temperature perturbations in chemistry-climate models. *Journal of Advances in Modeling Earth Systems*, *15*(9), e2022MS003505. https://doi.org/10.1029/2022ms003505

Wright, C. J. (2019). Quantifying the global impact of tropical cyclone-associated gravity waves using HIRDLS, MLS, SABER and IBTrACS data. *Quarterly Journal of the Royal Meteorological Society*, *145*(724), 3023–3039. https://doi.org/10.1002/qj.3602

Yook, S. (2024). Replication Data and Simulation Setups for: Dataset used to generate figures in "Implementation of sub-grid scale temperature perturbations induced by non-orographic gravity waves in WACCM6 [Dataset]. *Harvard Dataverse*. https://doi.org/10.7910/DVN/KC3VUQ

Zhang, G. J., & McFarlane, N. A. (1995). Role of convective scale momentum transport in climate simulation. *Journal of Geophysical Research*, *100*(D1), 1417–1426. https://doi.org/10.1029/94jd02519

Zou, L., Hoffmann, L., Griessbach, S., Spang, R., & Wang, L. (2021). Empirical evidence for deep convection being a major source of stratospheric ice clouds over North America. *Atmospheric Chemistry and Physics*, *21*(13), 10457–10475. https://doi.org/10.5194/acp-21-10457-2021